

Antiferromagnetic and bond-order-wave phases in the half-filled two-dimensional optical Su-Schrieffer-Heeger-Hubbard model

Andy Tanjaroon Ly^{1,2}, Benjamin Cohen-Stead^{1,2} and Steven Johnston^{1,2}

¹*Department of Physics and Astronomy, The University of Tennessee, Knoxville, TN 37996, USA*

²*Institute for Advanced Materials and Manufacturing, The University of Tennessee, Knoxville, TN 37996, USA*

Electron-phonon (e -ph) interactions arise in many strongly correlated quantum materials from the modulation of the nearest-neighbor hopping integrals, as in the celebrated Su-Schrieffer-Heeger (SSH) model. Nevertheless, relatively few non-perturbative studies of correlated SSH models have been conducted in dimensions greater than one, and those that have been done have primarily focused on bond models, where generalized displacements independently modulate each hopping integral. We conducted a sign-problem free determinant quantum Monte Carlo study of the optical SSH-Hubbard model on a two-dimensional square lattice, where site-centered phonon modes simultaneously modulate pairs of nearest-neighbor hopping integrals. We report the model's low-temperature phase diagram in the challenging adiabatic regime ($\Omega/E_F \sim 1/8$). It exhibits insulating antiferromagnetic Mott and bond-order-wave (BOW) phases with a narrow region of coexistence between them. We also find that a critical e -ph coupling is required to stabilize the BOW phase in the small U limit. Lastly, in stark contrast to recent findings for the model's bond variant, we find no evidence for a long-range antiferromagnetism in the pure ($U/t = 0$) optical SSH model.

I. INTRODUCTION

Strongly correlated quantum materials are often governed by the interplay between two or more degrees of freedom, which compete or cooperate with one another to produce novel states of matter and complex phase diagrams [1–4]. For example, many interesting phases can be derived from combining electron-phonon (e -ph) and electron-electron (e - e) interactions. A canonical model for this physics is the half-filled Hubbard-Holstein model, which hosts charge-density-wave, antiferromagnetic (AFM), and intermediate metallic phases, with the latter depending on the dimensionality of the system [5–12]. There is also evidence suggesting that e -ph interactions can enhance d -wave pairing [9, 13, 14] and affect spin and charge correlations [15, 16] in doped Hubbard-Holstein models.

Recently, interest in e -ph interactions has shifted toward SSH models, where the atomic motion modulates the electronic hopping integrals [17, 18]. While different variants of the SSH model have been introduced over the years, a widely studied one is the so-called “bond” SSH (bSSH) model [19], which places independent harmonic oscillators on the bonds between atomic sites. Quantum Monte Carlo (QMC) studies of the bSSH model have yielded interesting results regarding superconductivity [20, 21] and magnetism, including the presence of antiferromagnetism absent a Coulomb interaction [22, 23]. Subsequent work reported on the robustness of this anomalous antiferromagnetism and its competition with a bond-order-wave (BOW) phase, both with and without a Hubbard interaction [24–26]. A lesser studied variant is the “optical” SSH (oSSH) model [27], which instead places dispersionless Einstein phonons on the atomic sites that simultaneously modulate all of the surrounding nearest-neighbor hopping integrals. Recent determinant quantum Monte Carlo (DQMC) studies

have shown that the two models produce quite different physical results [28, 29], which motivates studies into correlated oSSH models. This class of interactions has also been implicated in a wide range of quantum materials [30–35].

This article presents a detailed study of the low temperature phases of the oSSH-Hubbard model on a square lattice using numerically exact DQMC. Both the oSSH and bSSH couplings preserve particle-hole symmetry at half-filling such that the simulations remain sign-problem-free, unlike in the Hubbard-Holstein model [8]. Focusing on the adiabatic regime ($\Omega/E_F \sim 1/8$) relevant to most materials, we obtain a low-temperature phase diagram with $\mathbf{Q} = (\pi/a, \pi/a)$ AFM and BOW phases, depending on the relative strengths of the e - e and e -ph interactions. We also find evidence for a narrow region of coexistence between these phases. At $T = 0$, the AFM and BOW phases are insulating; however, we find a small region of metallic behavior for small values of (λ, U) at finite temperatures but no indications of enhanced superconductivity in this region. Importantly, we also find no evidence for an AFM phase in the pure oSSH model ($U = 0$), in contrast to the bSSH model [22, 23]. Instead, we find only a weak enhancement of short-range AFM correlations in this region of parameter space. Our results highlight crucial differences between the two variants of the SSH model and how it competes with Mott correlations.

II. MODEL & METHODS

We study the oSSH-Hubbard model defined on two-dimensional $N = L \times L$ square lattices with periodic boundary conditions. Unlike the more commonly studied bond model [19], our model places the phonons on the sites [27] such that each displacement simultaneously

modulates two neighboring bonds rather than one. The model's Hamiltonian is

$$\hat{H} = \hat{H}_e + \hat{H}_{\text{ph}} + \hat{H}_U + \hat{H}_{e-\text{ph}}, \quad (1)$$

where

$$\hat{H}_e = -t \sum_{i,\nu,\sigma} (\hat{c}_{i+\mathbf{a}_\nu,\sigma}^\dagger \hat{c}_{i,\sigma} + \text{H.c.}) - \mu \sum_{i,\sigma} \hat{n}_{i,\sigma} \quad (2)$$

are the non-interacting electron terms,

$$\hat{H}_{\text{ph}} = \sum_{i,\nu} \left(\frac{1}{2M} \hat{P}_{i,\nu}^2 + \frac{M\Omega^2}{2} \hat{X}_{i,\nu}^2 \right) \quad (3)$$

are the non-interacting phonon terms,

$$\hat{H}_U = U \sum_i \hat{n}_{i,\uparrow} \hat{n}_{i,\downarrow} \quad (4)$$

is the Hubbard interaction, and

$$\hat{H}_{e-\text{ph}} = \alpha \sum_{i,\nu,\sigma} (\hat{X}_{i+\mathbf{a}_\nu,\nu} - \hat{X}_{i,\nu}) (\hat{c}_{i+\mathbf{a}_\nu,\sigma}^\dagger \hat{c}_{i,\sigma} + \text{H.c.}). \quad (5)$$

is the e -ph interaction. In Eqs. (2)-(5), $\hat{c}_{i,\sigma}^\dagger$ ($\hat{c}_{i,\sigma}$) creates (annihilates) a spin- σ ($=\uparrow, \downarrow$) electron at lattice site i , $\hat{n}_{i,\sigma} = \hat{c}_{i,\sigma}^\dagger \hat{c}_{i,\sigma}$ is the number operator, and H.c. denotes the Hermitian conjugate. The index ν runs over the \hat{x} and \hat{y} spatial dimensions, and $\mathbf{a}_x = (a, 0)$ and $\mathbf{a}_y = (0, a)$ are the primitive lattice vectors of the square lattice. t is the nearest neighbor hopping integral, μ is the chemical potential, U is the Hubbard repulsion, M is the ion mass, and $\hbar\Omega$ is the phonon energy. Lastly, $\hat{X}_{i,\nu}$ ($\hat{P}_{i,\nu}$) is the position (momentum) operator for the atom at site i along the $\nu = \hat{x}, \hat{y}$ directions, and α controls the e -ph coupling strength.

We solve Eq (1) using numerically exact DQMC, as implemented in the `SmoQyDQMC.jl` package [36–38]. Throughout this work, we focus on half-filling $\langle n \rangle = 1$, and take $t = M = a = \hbar = 1$ to set our units of measurement. We further fix $\Omega = t/2$ unless otherwise stated and adopt a Brillouin zone-averaged definition of the dimensionless coupling

$$\lambda = \frac{2}{WN^2} \sum_{\mathbf{k}, \mathbf{q}, \nu} \frac{|g_\nu(\mathbf{k}, \mathbf{q})|^2}{\Omega(\mathbf{q})} = \frac{8\alpha^2}{M\Omega^2 W}, \quad (6)$$

where $g_\nu(\mathbf{k}, \mathbf{q})$ is the e -ph matrix element for phonon branch ν , $W = 8t$ is the non-interacting bandwidth, and $E_F = 4t$ is the Fermi energy. We refer the reader to Refs. [28, 29] for further discussion on defining λ and the explicit form of $g(\mathbf{k}, \mathbf{q})$.

We assess the model's ordering tendencies by measuring the susceptibilities

$$\chi_\gamma(\mathbf{q}) = \int_0^\beta S_\gamma(\mathbf{q}, \tau) d\tau, \quad (7)$$

where γ indexes the spin (s), bond (b), or pairing (p) correlations and

$$S_\gamma(\mathbf{q}, \tau) = \frac{1}{N} \sum_{i,j} e^{-i\mathbf{q}\cdot(\mathbf{R}_i - \mathbf{R}_j)} \left\langle \hat{O}_{\gamma,i}(\tau) \hat{O}_{\gamma,j}^\dagger(0) \right\rangle \quad (8)$$

is the corresponding structure factor. The relevant operators are

$$\hat{O}_{s,i} = \frac{1}{2} (\hat{n}_{i,\uparrow} - \hat{n}_{i,\downarrow}), \quad (9)$$

for AFM correlations,

$$\hat{O}_{b,i} = \frac{1}{2} \sum_\sigma (\hat{c}_{i,\sigma}^\dagger \hat{c}_{i+\mathbf{a}_\nu,\sigma} + \text{H.c.}), \quad (10)$$

for bond correlations and

$$\hat{O}_{p,i} = \hat{c}_{i,\uparrow} \hat{c}_{i,\downarrow}, \quad (11a)$$

$$\hat{O}_{p,i}^{s*} = \frac{1}{2} \sum_\nu (\hat{c}_{i,\uparrow} \hat{c}_{i+\mathbf{a}_\nu,\downarrow} + \hat{c}_{i,\uparrow} \hat{c}_{i-\mathbf{a}_\nu,\downarrow}), \quad \text{and} \quad (11b)$$

$$\hat{O}_{p,i}^d = \frac{1}{2} \sum_\nu \mathcal{P}_\nu (\hat{c}_{i,\uparrow} \hat{c}_{i+\mathbf{a}_\nu,\downarrow} + \hat{c}_{i,\uparrow} \hat{c}_{i-\mathbf{a}_\nu,\downarrow}) \quad (11c)$$

for the superconducting correlations with s -, extended s -, and d -wave symmetries, respectively. Here, $\mathcal{P}_\nu = (\delta_{x,\nu} - \delta_{y,\nu})$ is a phase factor for the d -wave symmetry.

To assess critical behavior, we compute the correlation ratio from the equal-time structure factors

$$R_\gamma(L) = 1 - \frac{S_\gamma(\mathbf{Q} - \delta\mathbf{q}_L, 0)}{S_\gamma(\mathbf{Q}, 0)},$$

where L denotes the cluster size, $|\delta\mathbf{q}_L| = \frac{2\pi}{La}$ and $\mathbf{Q} = (\pi/a, \pi/a)$ is the ordering wave for both the AFM and BOW correlations. The critical point for the transition can then be determined from the crossing point of the $R_\gamma(L)$ curves for different lattice sizes while fixing $\beta = L$ to access low-temperature (ground state) properties [39–42]. We also performed measurements of other standard quantities, such as the double occupancy and average electron kinetic energy

$$\langle K_\nu \rangle = - \left\langle t (\hat{X}_{i+\mathbf{a}_\nu,\nu} - \hat{X}_{i,\nu}) \hat{c}_{i+\mathbf{a}_\nu,\sigma}^\dagger \hat{c}_{i,\sigma} + \text{H.c.} \right\rangle. \quad (12)$$

When computing the local observables, we bias the system for the x -bonds to ensure that we select the same broken symmetry state.

III. RESULTS

Figure 1 plots the low-temperature phase diagram of the half-filled oSSH-Hubbard model in the λ - U plane. For small e -ph coupling, the system is dominated by AFM Mott/Slater correlations depending

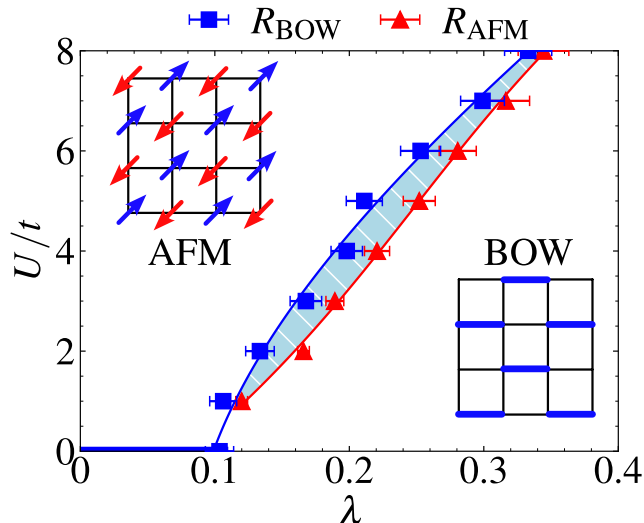


FIG. 1. Phase diagram of the optical SSH-Hubbard model at half-filling $\langle n \rangle = 1$ with a fixed phonon frequency $\Omega/t = 0.5$. The red triangles and blue squares denote the transition points obtained from AFM and BOW correlation ratios, respectively, with solid lines providing a guide for the eye. The blue hatched area represents the region of AFM/BOW coexistence. The thick blue line from $\lambda = 0$ to λ_c along the $U = 0$ line denotes a region where the pure optical SSH model has no long-range AFM or BOW order.

on the value of U/t . Increasing the e -ph coupling for fixed U/t drives the system into a non-magnetic insulating BOW phase, with a narrow intermediate regime of AFM/BOW coexistence, as indicated by the hatched shading. Additionally, in the $U/t = 0$ limit, the BOW ground state disappears below a critical coupling $\lambda_c^{\text{BOW}} = 0.103 \pm 0.010$. Below this coupling, we observe a weak enhancement of the short-range AFM correlations in the pure oSSH model but no long-range AFM order. This result is in direct contrast with the bSSH model, where long-range magnetic order was reported [22, 23]. We can understand this result by considering the difference in the effective e - e interactions that arise in the anti-adiabatic limits of the two models, see Supplementary Note 1 [43]. We also estimate that for $\lambda < \lambda_c^{\text{BOW}}$ and $U/t \lesssim 2$, the system is an AFM metal at elevated temperatures ($\beta \geq 16/t$, see Supplementary Note 2) before transitioning to an insulator at higher U/t or lower temperatures. In the following sections, we will discuss the various measurements that lead to this phase diagram.

The phase boundaries in Fig. 1 were obtained from the crossing point of the BOW and AFM correlation ratios, as illustrated in Fig. 2. Here we show the correlation ratio for BOW and AFM order in Figs 2a and 2b, respectively, for a representative value of $U/t = 3$. This analysis is based on a finite-size scaling analysis [40–

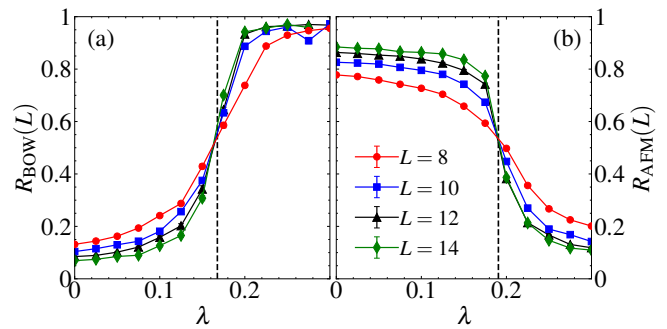


FIG. 2. Correlation ratios for the (a) bond-ordered-wave and (b) antiferromagnetic phases as a function of λ for fixed $U/t = 3$. The location of the quantum critical point λ_c is obtained from the crossing of the correlation ratio for different lattice sizes L and is indicated by the dashed lines. All calculations were performed for fixed phonon frequency $\Omega/t = 0.5$ and at an inverse temperature $\beta t = L$. The definition of the correlation ratio is provided in the Methods section.

42], where the quantum critical point (QCP) λ_c corresponds to the crossing point of the $R_\gamma(L)$ curves for different cluster sizes L while fixing $\beta t = L$. This approach assumes that the dynamical critical exponent for the AFM and BOW transitions is $z = 1$ [12, 44]. In this case, we obtain $\lambda_c^{\text{BOW}} = 0.16 \pm 0.01$ (see Fig. 2a) and $\lambda_c^{\text{AFM}} = 0.189 \pm 0.007$ (see Fig. 2b). The difference in these values suggests a narrow region of coexistence between the two states, where BOW order has begun to set in while AFM order has not yet disappeared. This result is distinct from that of the bSSH and bSSH-Hubbard models, in which a direct transition from a BOW to AFM ground state occurs, with no reported region of coexistence [22–25]. The remaining points in Fig. 1 were obtained from a similar analysis, as shown in Supplementary Note 3 [43].

Another key difference between our phase diagram and results obtained for the bSSH model pertains to the behavior along the $U/t = 0$ line. In the pure bSSH model, AFM order is stabilized without a Hubbard interaction [22]. Here, however, we observe no such order along the $U/t = 0$ line but instead only a weak enhancement of short-range AFM correlations, see Supplementary Note 4. This behavior is illustrated in Figs. 3a and 3b, which plot the BOW and AFM correlation ratios in this limit, respectively. While we obtain a finite critical coupling for the BOW phase from the corresponding correlation ratio crossing, we observe no similar crossing in AFM correlation ratio. Taking a larger $\Omega/t = 2$ produces similar results, as shown in Figs. 3c and 3d, with $\lambda_c = 0.130 \pm 0.004$ for the BOW transition and no crossing for the AFM correlation ratio. The similarity of the results in Figs. 3b and 3d suggest that the absence of AFM order is due to the nature of the oSSH coupling rather than the phonon energy.

The lack of AFM order in the oSSH model can be understood by considering the effective e - e interaction

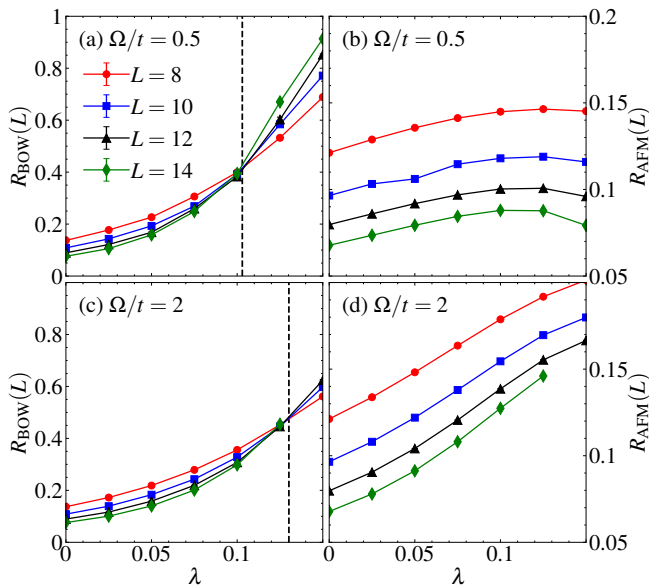


FIG. 3. Correlation ratios for the bond-ordered-wave and antiferromagnetic orders as a function of λ for the pure oSSH model ($U/t = 0$) at $\Omega/t = 0.5$ [panels (a) and (b)] and $\Omega/t = 2$ [panels (c) and (d)]. The BOW data indicates there is a finite critical coupling $\lambda_c(\Omega/t = 0.5) = 0.103 \pm 0.010$ and $\lambda_c(\Omega/t = 2) = 0.130 \pm 0.004$, while no crossing point is observed for the AFM correlations. All calculations were performed at an inverse temperature $\beta t = L$.

that arises in the anti-adiabatic limit. Previous studies showed that in this limit, the bSSH model gives rise to a Heisenberg-like nearest-neighbor coupling between the electron spins that favors AFM correlations [22, 23]. In Supplementary Note 1, we show that while the anti-adiabatic oSSH model retains this nearest-neighbor $e-e$ interaction, it also introduces longer-range interactions of similar strength between electrons on the same sublattice [43]. These longer-range interactions frustrate any AFM correlations from occurring. Intuitively, this difference in the effective $e-e$ interaction arises from the fact that each phonon mode in the oSSH model modulates two hopping integrals as opposed to just one, as in the bSSH model.

Our scaling analysis of the crossing ratio fixed $\beta = L$ to access low-temperature (ground state) properties. It is possible that our simulations are not reaching low enough temperatures to access the true ground state and that AFM does ultimately appear at lower temperatures. However, our results clearly show that if this is the case, the transition temperature is much lower in the oSSH model than in the bSSH model. This result is consistent with the presence of frustrating next-nearest neighbor interactions, as discussed in Supplementary Note 1. Ground state calculations would be valuable in this context.

To further examine the relevant transitions between

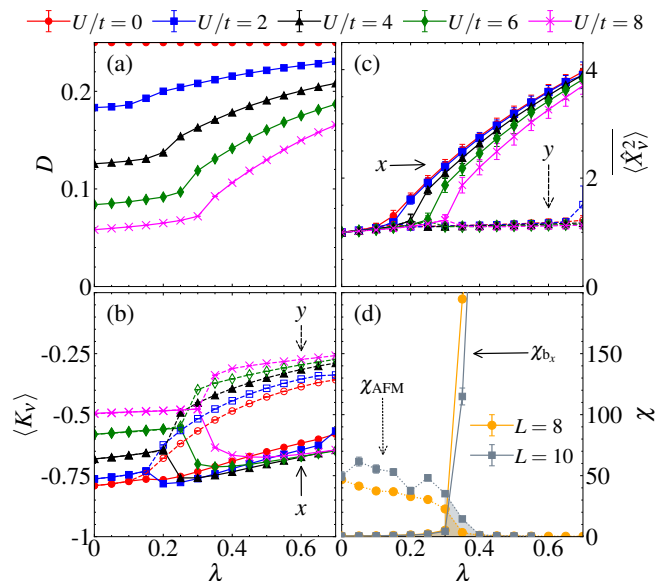


FIG. 4. A summary of several local observables for the optical SSH-Hubbard model. (a) the average double occupancy D . (b) the average kinetic energy $\langle K_\nu \rangle$ in the \hat{x} (solid lines) and \hat{y} (dashed lines) directions. (c) the root mean square of the average displacement $(\langle \hat{X}_\nu^2 \rangle)^{1/2}$ in the \hat{x} and \hat{y} -directions. (d) a comparison of the AFM (dotted lines) and x -direction BOW (solid lines) susceptibilities for fixed $U/t = 8$ at $L = 8$ (orange circles) and $L = 10$ (gray squares). The shaded area indicates the region of AFM/BOW coexistence. All results were obtained for $\Omega/t = 0.5$, $\beta t = 16$, and $\langle n \rangle = 1$. The results in panels a-c were obtained on $L = 8$ clusters.

AFM and BOW order and the possible coexistence region, we measured several local observables on $L = 8$ clusters at low temperature ($\beta t = 16$). Local observables are often sensitive to changes in the dominant correlations in the system while being less prone to finite size effects [8, 12, 36].

Figure 4a shows the average double occupancy $D = \langle n_{i,\uparrow} n_{i,\downarrow} \rangle$ as a function of λ for selected values of U/t . Mott correlations for weak couplings initially suppress the double occupancy, but it grows as the strength of the e -ph coupling increases. Notably, the D vs. λ curves have a kink at λ values that coincide with the transition from the AFM to BOW state, as indicated by the red line in Fig. 1. For larger values of λ , the values of the double occupancies begin growing toward their uncorrelated values, which reflects the increased hybridization between pairs of sites in the BOW phase.

The average values of the electron kinetic energy $\langle \hat{K}_\nu \rangle$ and the root mean square phonon displacement $(\langle \hat{X}_\nu^2 \rangle)^{1/2}$ are shown in Figs. 4b and 4c, respectively. Because the SSH interaction modulates the nearest-neighbor hopping integrals, both quantities indicate how strongly the lattice distorts across parameter space. We observe a bifurcation in both at coupling values that approximately coincide with BOW transition line shown

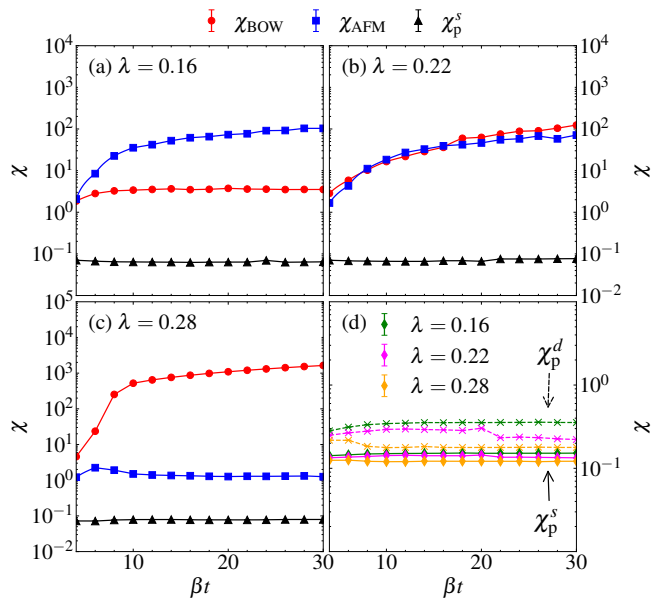


FIG. 5. Finite temperature susceptibilities in different regions of the phase diagram. Panels (a), (b), and (c) show AFM (blue squares), BOW (red circles), and on-site s -wave pairing (black triangles) susceptibilities at $\lambda = 0.16, 0.22$, and 0.28 , respectively. Panel (d) plots the corresponding extended s - (χ_p^s , solid lines) and d -wave (χ_p^d , dashed lines) susceptibilities. Lines are a guide to the eye. All results were obtained from $L = 14$ lattices with fixed $U/t = 4.5$, $\Omega = t/2$, and $\langle n \rangle = 1$.

in Fig. 1. The average electron kinetic energy and root mean square phonon displacement measured along each crystallographic direction are equal in the AFM phase but split in the BOW phase. This bifurcation is also observed in bSSH models [22, 28, 45] and reflects the broken C_4 symmetry of the BOW phase, sketched in the right inset of Fig. 1.

Finally, Fig. 4d examines the AFM and BOW susceptibilities for $U/t = 8$ and $L = 8$ and 10 clusters. Here, we observe a small region where both susceptibilities have large non-zero values, as indicated by the shaded area. This behavior is consistent with coexistence between the AFM and BOW phases.

Next, we examine the temperature dependence of the AFM, BOW, and pairing susceptibilities χ_γ in different regions of the phase diagram. Fig. 5 plots the results on a log scale for $\lambda = 0.16, 0.22$, and 0.28 as a function of βt and fixed $U/t = 4.5$. These results were obtained on a larger $L = 14$ cluster. For $\lambda = 0.16$, we expect the system to be antiferromagnetic, which is corroborated by the dominant $\chi_s(\pi, \pi)$ at low-temperatures shown in Fig. 5a. Similarly, for $\lambda = 0.28$, we expect the system to be in a BOW phase, which is consistent with the dominant $\chi_b(\pi, \pi)$ shown in Fig. 5c. More interesting is the $\lambda = 0.22$ case, which lies within the coexistence region. In this case, the AFM and BOW susceptibilities are of the

same order of magnitude and grow concomitantly with decreasing temperature.

It has recently been shown that bSSH-like interactions can mediate strong binding between carriers in the dilute limit [46] and potential high-temperature superconductivity, provided that it is not preempted by the formation of any competing order [20, 21]. The black triangles in Figs. 5a-c plot the on-site s -wave pairing susceptibility as a function of temperature and give no indication of a superconducting instability. Fig 5d also plots the temperature dependence of the extended s -wave and d -wave susceptibilities for the three regions identified in the phase diagram. Here we find no indications of robust s -wave, extended s -wave, or d -wave pairing. While the d -wave susceptibility is the dominant pairing channel for all values of λ we have checked, its magnitude is several orders of magnitude smaller than either the AFM or BOW susceptibilities at low temperatures.

The AFM phase found at small U/t and λ is metallic at $\beta = 16/t$. We have found that insulating behavior sets in upon further cooling, and we have observed no indications of low-temperature superconducting correlations in this region of the phase diagram either. These results provide strong numerical evidence that the AFM or BOW phases are dominant at half-filling across the entire (λ, U) -plane as might be expected for such a commensurate filling. It remains to be seen whether doping the system, which will introduce a sign problem, will induce superconductivity; however, we also note that a recent study of the pure doped oSSH model, which does not have a sign problem, found no indication of high-temperature superconductivity for these parameters [28].

IV. DISCUSSION

We have conducted a detailed DQMC study of the magnetic and bond-ordered phases of the half-filled oSSH-Hubbard model in the (λ, U) -plane, focusing on the challenging adiabatic regime relevant to most materials. For weak e -ph coupling, the system is dominated by AFM Mott correlations similar to those observed in the single-band Hubbard model. Increasing the e -ph coupling strength above a non-zero U -dependent critical value λ_c^{BOW} induces a BOW phase. Additionally, while there is no sign of enhanced superconducting correlations anywhere in the phase diagram, we did find evidence for a narrow region of coexistence between the AFM and BOW phases. Finally, in the $U = 0$ limit, we did not detect any long-range AFM phase in the pure oSSH model. We did, however, observe a weak enhancement of AFM correlations in this regime, indicating that such correlations are short-ranged at the temperatures we accessed [43]. In this context, we note that any sign-problem-free-model is expect to have a low-temperature instability away from a Fermi-liquid ground state [47]. Thus we expect either superconductivity, antiferromag-

netism, or non-Fermi-liquid behavior at zero temperature. However, which instability ultimately occurs currently cannot be assessed from our result.

Previous DQMC studies of the bSSH-Hubbard model have also observed a transition between AFM and BOW phases [24, 25]. These studies focused on higher energy phonon modes ($\Omega = 3t/2$ in Ref. [24] and $\Omega = t$ in Ref. [25]) and considered a model where each hopping integral is modulated independently, unlike in our model. Neither study reported any evidence for a region of coexistence between the two orders. We believe this difference stems from the nature of the microscopic coupling [28, 29]. For example, in the anti-adiabatic limit, the bSSH model can generate AFM order through an effective nearest-neighbor Heisenberg-like interaction [22]. In contrast, the oSSH model introduces additional longer-range interaction terms which frustrate the AFM order [43]. The combination of both an effective nearest-neighbor Heisenberg-like interaction and longer-range frustrating interactions would also explain the presence of enhanced short-range AFM correlations but the absence of long-range AFM order. The bSSH model also has a non-zero coupling to the $\mathbf{q} = 0$ modes, which is forbidden in the case of the oSSH model [29]. The mobility of the oSSH polarons also appears to be much smaller than those of the bSSH model [28].

Understanding the interplay of e -ph and Coulomb interactions has implications for the study of many strongly correlated materials. While both the Hubbard-Holstein and the bSSH-Hubbard models have been explored numerically, the oSSH model has received com-

paratively less attention. With newer state-of-the-art numerical methods, we have successfully mapped out the principal phases of the half-filled oSSH-Hubbard model. In the future, it would be interesting to dope the system and study the differences in the superconducting correlations obtained from either the parent AFM or BOW phases.

Acknowledgments: A. T. L. would like to thank L. Rademaker for useful discussions and hospitality. This work was primarily supported by the National Science Foundation under Grant No. DMR-2401388. A. T. L. acknowledges additional support from the U.S. Department of Energy, Office of Science, Office of Workforce Development for Teachers and Scientists, Office of Science Graduate Student Research (SCGSR) program, during the writing phase of this project. The SCGSR program is administered by the Oak Ridge Institute for Science and Education (ORISE) for the DOE. ORISE is managed by ORAU under contract number DE-SC0014664. This research used resources of the Compute and Data Environment for Science (CADES) at the Oak Ridge National Laboratory, which is supported by the Office of Science of the U.S. Department of Energy under Contract No. DE-AC05-00OR22725.

Data Availability: The data supporting this study will be made available through a public repository once it is published. Until then, the data will be made available on request. The code supporting this study is available at: <https://github.com/SmoQySuite/SmoQyDQMC.jl>.

-
- [1] E. Dagotto, Complexity in strongly correlated electronic systems, *Science* **309**, 257 (2005).
 - [2] E. Morosan, D. Natelson, A. H. Nevidomskyy, and Q. Si, Strongly correlated materials, *Advanced Materials* **24**, 4896 (2012).
 - [3] J. C. S. Davis and D.-H. Lee, Concepts relating magnetic interactions, intertwined electronic orders, and strongly correlated superconductivity, *Proceedings of the National Academy of Sciences* **110**, 17623 (2013).
 - [4] E. Fradkin, S. A. Kivelson, and J. M. Tranquada, Colloquium: Theory of intertwined orders in high temperature superconductors, *Rev. Mod. Phys.* **87**, 457 (2015).
 - [5] R. T. Scalettar, N. E. Bickers, and D. J. Scalapino, Competition of pairing and Peierls-charge-density-wave correlations in a two-dimensional electron-phonon model, *Phys. Rev. B* **40**, 197 (1989).
 - [6] W. Koller, D. Meyer, Y. Ōno, and A. C. Hewson, First- and second-order phase transitions in the Holstein-Hubbard model, *Europhysics Letters* **66**, 559 (2004).
 - [7] P. Werner and A. J. Millis, Efficient dynamical mean field simulation of the Holstein-Hubbard model, *Phys. Rev. Lett.* **99**, 146404 (2007).
 - [8] S. Johnston, E. A. Nowadnick, Y. F. Kung, B. Moritz, R. T. Scalettar, and T. P. Devereaux, Determinant quantum Monte Carlo study of the two-dimensional single-band Hubbard-Holstein model, *Phys. Rev. B* **87**, 235133 (2013).
 - [9] E. A. Nowadnick, S. Johnston, B. Moritz, and T. P. Devereaux, Renormalization of spectra by phase competition in the half-filled Hubbard-Holstein model, *Phys. Rev. B* **91**, 165127 (2015).
 - [10] S. Karakuzu, L. F. Tocchio, S. Sorella, and F. Becca, Superconductivity, charge-density waves, antiferromagnetism, and phase separation in the Hubbard-Holstein model, *Phys. Rev. B* **96**, 205145 (2017).
 - [11] Y. Wang, I. Esterlis, T. Shi, J. I. Cirac, and E. Demler, Zero-temperature phases of the two-dimensional Hubbard-Holstein model: A non-Gaussian exact diagonalization study, *Phys. Rev. Res.* **2**, 043258 (2020).
 - [12] N. C. Costa, K. Seki, S. Yunoki, and S. Sorella, Phase diagram of the two-dimensional Hubbard-Holstein model, *Communications Physics* **3**, 80 (2020).
 - [13] R. Zeyher and M. L. Kulić, Renormalization of the electron-phonon interaction by strong electronic correlations in high- T_c superconductors, *Phys. Rev. B* **53**, 2850 (1996).
 - [14] Z. B. Huang, W. Hanke, E. Arrighoni, and D. J. Scalapino, Electron-phonon vertex in the two-dimensional one-band

- Hubbard model, *Phys. Rev. B* **68**, 220507 (2003).
- [15] S. Karakuzu, A. Tanjaroon Ly, P. Mai, J. Neuhaus, T. A. Maier, and S. Johnston, Stripe correlations in the two-dimensional Hubbard-Holstein model, *Communications Physics* **5**, 311 (2022).
- [16] J. Liu, S. Li, E. W. Huang, and Y. Wang, Charge density wave state in extremely overdoped cuprates driven by phonons, *Phys. Rev. B* **110**, 115133 (2024).
- [17] S. Barišić, J. Labbé, and J. Friedel, Tight binding and transition-metal superconductivity, *Phys. Rev. Lett.* **25**, 919 (1970).
- [18] W. P. Su, J. R. Schrieffer, and A. J. Heeger, Solitons in polyacetylene, *Phys. Rev. Lett.* **42**, 1698 (1979).
- [19] P. Sengupta, A. W. Sandvik, and D. K. Campbell, Peierls transition in the presence of finite-frequency phonons in the one-dimensional extended Peierls-Hubbard model at half-filling, *Phys. Rev. B* **67**, 245103 (2003).
- [20] C. Zhang, J. Sous, D. R. Reichman, M. Berciu, A. J. Millis, N. V. Prokof'ev, and B. V. Svistunov, Bipolaronic high-temperature superconductivity, *Phys. Rev. X* **13**, 011010 (2023).
- [21] X. Cai, Z.-X. Li, and H. Yao, High-temperature superconductivity induced by the Su-Schrieffer-Heeger electron-phonon coupling, [arXiv:2308.06222](https://arxiv.org/abs/2308.06222) (2023).
- [22] X. Cai, Z.-X. Li, and H. Yao, Antiferromagnetism Induced by bond Su-Schrieffer-Heeger electron-phonon coupling: A quantum Monte Carlo study, *Phys. Rev. Lett.* **127**, 247203 (2021).
- [23] A. Götz, S. Beyl, M. Hohenadler, and F. F. Assaad, Valence-bond solid to antiferromagnet transition in the two-dimensional Su-Schrieffer-Heeger model by Langevin dynamics, *Phys. Rev. B* **105**, 085151 (2022).
- [24] X. Cai, Z.-X. Li, and H. Yao, Robustness of antiferromagnetism in the Su-Schrieffer-Heeger Hubbard model, *Phys. Rev. B* **106**, L081115 (2022).
- [25] C. Feng, B. Xing, D. Poletti, R. Scalettar, and G. Batrouni, Phase diagram of the Su-Schrieffer-Heeger-Hubbard model on a square lattice, *Phys. Rev. B* **106**, L081114 (2022).
- [26] B. Xing, C. Feng, R. Scalettar, G. G. Batrouni, and D. Poletti, Attractive Su-Schrieffer-Heeger-Hubbard model on a square lattice away from half-filling, *Phys. Rev. B* **108**, L161103 (2023).
- [27] M. Capone, W. Stephan, and M. Grilli, Small-polaron formation and optical absorption in Su-Schrieffer-Heeger and Holstein models, *Phys. Rev. B* **56**, 4484 (1997).
- [28] A. Tanjaroon Ly, B. Cohen-Stead, S. Malkaruge Costa, and S. Johnston, Comparative study of the superconductivity in the Holstein and optical Su-Schrieffer-Heeger models, *Phys. Rev. B* **108**, 184501 (2023).
- [29] S. Malkaruge Costa, B. Cohen-Stead, A. Tanjaroon Ly, J. Neuhaus, and S. Johnston, Comparative determinant quantum Monte Carlo study of the acoustic and optical variants of the Su-Schrieffer-Heeger model, *Phys. Rev. B* **108**, 165138 (2023).
- [30] G.-m. Zhao, K. Conder, M. Angst, S. M. Kazakov, J. Karpinski, M. Maciejewski, C. Bougerol, J. S. Pshirkov, and E. V. Antipov, Large oxygen-isotope effect in $\text{Sr}_{0.4}\text{K}_{0.6}\text{BiO}_3$: Evidence for phonon-mediated superconductivity, *Phys. Rev. B* **62**, R11977 (2000).
- [31] T. P. Devereaux, T. Cuk, Z.-X. Shen, and N. Nagaosa, Anisotropic electron-phonon interaction in the cuprates, *Phys. Rev. Lett.* **93**, 117004 (2004).
- [32] S. Johnston, F. Vernay, B. Moritz, Z.-X. Shen, N. Nagaosa, J. Zaanen, and T. P. Devereaux, Systematic study of electron-phonon coupling to oxygen modes across the cuprates, *Phys. Rev. B* **82**, 064513 (2010).
- [33] B. Cohen-Stead, O. Bradley, C. Miles, G. Batrouni, R. Scalettar, and K. Barros, Fast and scalable quantum Monte Carlo simulations of electron-phonon models, *Phys. Rev. E* **105**, 065302 (2022).
- [34] C. Zhang, L. W. Harriger, Z. Yin, W. Lv, M. Wang, G. Tan, Y. Song, D. L. Abernathy, W. Tian, T. Egami, K. Haule, G. Kotliar, and P. Dai, Effect of pnictogen height on spin waves in iron pnictides, *Phys. Rev. Lett.* **112**, 217202 (2014).
- [35] S. Johnston, A. Mukherjee, I. Elfimov, M. Berciu, and G. A. Sawatzky, Charge disproportionation without charge transfer in the rare-earth-element nickelates as a possible mechanism for the metal-insulator transition, *Phys. Rev. Lett.* **112**, 106404 (2014).
- [36] S. R. White, D. J. Scalapino, R. L. Sugar, E. Y. Loh, J. E. Gubernatis, and R. T. Scalettar, Numerical study of the two-dimensional Hubbard model, *Phys. Rev. B* **40**, 506 (1989).
- [37] B. Cohen-Stead, S. Malkaruge Costa, J. Neuhaus, A. Tanjaroon Ly, Y. Zhang, R. Scalettar, K. Barros, and S. Johnston, SmoQyDQMC.jl: A flexible implementation of determinant quantum Monte Carlo for Hubbard and electron-phonon interactions, *SciPost Phys. Codebases* , 29 (2024).
- [38] B. Cohen-Stead, S. Malkaruge Costa, J. Neuhaus, A. Tanjaroon Ly, Y. Zhang, R. Scalettar, K. Barros, and S. Johnston, Codebase release r0.3 for SmoQyDQMC.jl, *SciPost Phys. Codebases* , 29 (2024).
- [39] R. K. Kaul, Spin nematics, valence-bond solids, and spin liquids in $\text{SO}(N)$ quantum spin models on the triangular lattice, *Phys. Rev. Lett.* **115**, 157202 (2015).
- [40] T. Sato, F. F. Assaad, and T. Grover, Quantum Monte Carlo simulation of frustrated Kondo lattice models, *Phys. Rev. Lett.* **120**, 107201 (2018).
- [41] Z. H. Liu, X. Y. Xu, Y. Qi, K. Sun, and Z. Y. Meng, Itinerant quantum critical point with frustration and a non-fermi liquid, *Phys. Rev. B* **98**, 045116 (2018).
- [42] A. S. Darmawan, Y. Nomura, Y. Yamaji, and M. Imada, Stripe and superconducting order competing in the Hubbard model on a square lattice studied by a combined variational Monte Carlo and tensor network method, *Phys. Rev. B* **98**, 205132 (2018).
- [43] See online supplementary materials.
- [44] A. Götz, M. Hohenadler, and F. F. Assaad, Phases and exotic phase transitions of a two-dimensional Su-Schrieffer-Heeger model, *Phys. Rev. B* **109**, 195154 (2024).
- [45] M. Casebolt, C. Feng, R. T. Scalettar, S. Johnston, and G. G. Batrouni, Magnetic, charge, and bond order in the two-dimensional Su-Schrieffer-Heeger-Holstein model, *Phys. Rev. B* **110**, 045112 (2024).
- [46] J. Sous, M. Chakraborty, R. V. Krems, and M. Berciu, Light bipolarons stabilized by Peierls electron-phonon coupling, *Phys. Rev. Lett.* **121**, 247001 (2018).
- [47] O. Grossman and E. Berg, Robust Fermi-Liquid Instabilities in Sign Problem-Free Models, *Phys. Rev. Lett.* **131**, 056501 (2023).

Supplementary materials for “Antiferromagnetic and bond-order-wave phases in the half-filled two-dimensional optical Su-Schrieffer-Heeger-Hubbard model”

Andy Tanjaroon Ly^{1,2}, Benjamin Cohen-Stead^{1,2} and Steven Johnston^{1,2}

¹*Department of Physics and Astronomy, The University of Tennessee, Knoxville, TN 37996, USA*

²*Institute for Advanced Materials and Manufacturing, The University of Tennessee, Knoxville, TN 37996, USA*

(Dated: February 21, 2025)

Supplementary Note 1: Effective interaction in the anti-adiabatic limit

The action of the “optical” SSH (oSSH) model on the imaginary time axis is given by

$$S[\bar{\psi}, \psi, X] = \int d\tau \sum_{i,\nu} \left[\bar{\psi} \partial_\tau \psi - t \hat{B}_{i,i+\mathbf{a}_\nu} + \frac{M}{2} \left(\partial_\tau \hat{X}_{i,\nu} \right)^2 + \frac{K}{2} X_{i,\nu}^2 + \alpha \left(\hat{X}_{i+\mathbf{a}_\nu,\nu} - \hat{X}_{i,\nu} \right) \hat{B}_{i,i+\mathbf{a}_\nu} \right],$$

where ν runs over the \hat{x} and \hat{y} spatial dimensions. Here, $\mathbf{a}_x = (a, 0)$ and $\mathbf{a}_y = (0, a)$ are the primitive lattice vectors, $\hat{X}_{i,\nu}$ is the position operator for the atom at site \mathbf{i} along each of the directions ν of the lattice, and $\hat{B}_{i,i+\mathbf{a}_\nu} = \sum_\sigma (\bar{\psi}_i \psi_{i+\mathbf{a}_\nu} + \text{H.c.})$ is the bond operator between lattice sites \mathbf{i} and $\mathbf{i} + \mathbf{a}_\nu$.

In the anti-adiabatic limit, $M \rightarrow 0$ (or $\Omega \rightarrow \infty$) and the phonon kinetic term drops out of the integral

$$S[\bar{\psi}, \psi, X] = \int d\tau \sum_{i,\nu} \left[\bar{\psi} \partial_\tau \psi - t \hat{B}_{i,i+\mathbf{a}_\nu} + \frac{K}{2} X_{i,\nu}^2 + \alpha \left(\hat{X}_{i+\mathbf{a}_\nu,\nu} - \hat{X}_{i,\nu} \right) \hat{B}_{i,i+\mathbf{a}_\nu} \right].$$

Next, we redefine the electron-phonon (e -ph) interaction term to an equivalent form

$$\sum_{i,\nu} \alpha \left(\hat{X}_{i+\mathbf{a}_\nu,\nu} - \hat{X}_{i,\nu} \right) \hat{B}_{i,i+\mathbf{a}_\nu} = \sum_{i,\nu} \alpha \hat{X}_{i,\nu} \left(\hat{B}_{i,i+\mathbf{a}_\nu} - \hat{B}_{i,i-\mathbf{a}_\nu} \right).$$

This form allows us to complete the square and obtain

$$\begin{aligned} S[\bar{\psi}, \psi, X] &= \int d\tau \sum_{i,\nu} \left[\bar{\psi} \partial_\tau \psi - t \hat{B}_{i,i+\mathbf{a}_\nu} + \frac{K}{2} X_{i,\nu}^2 + \alpha \hat{X}_{i,\nu} \left(\hat{B}_{i,i+\mathbf{a}_\nu} - \hat{B}_{i,i-\mathbf{a}_\nu} \right) \right] \\ &= \int d\tau \sum_{i,\nu} \left\{ \bar{\psi} \partial_\tau \psi - t \hat{B}_{i,i+\mathbf{a}_\nu} + \frac{K}{2} \left[X_{i,\nu} + \frac{\alpha}{K} \left(\hat{B}_{i,i+\mathbf{a}_\nu} - \hat{B}_{i,i-\mathbf{a}_\nu} \right) \right]^2 - \frac{\alpha^2}{K} \left(\hat{B}_{i,i+\mathbf{a}_\nu} - \hat{B}_{i,i-\mathbf{a}_\nu} \right)^2 \right\} \\ &= \int d\tau \sum_{i,\nu} \left[\bar{\psi} \partial_\tau \psi - t \hat{B}_{i,i+\mathbf{a}_\nu} - \frac{\alpha^2}{K} \left(\hat{B}_{i,i+\mathbf{a}_\nu} - \hat{B}_{i,i-\mathbf{a}_\nu} \right)^2 \right], \end{aligned}$$

where we have explicitly integrated out the phonons in the last step. Expanding the $\left(\hat{B}_{i,i+\mathbf{a}_\nu} - \hat{B}_{i,i-\mathbf{a}_\nu} \right)^2$ term, we then obtain

$$\begin{aligned} S[\bar{\psi}, \psi, X] &= \int d\tau \sum_{i,\nu} \left[\bar{\psi} \partial_\tau \psi - t \hat{B}_{i,i+\mathbf{a}_\nu} - \frac{\alpha^2}{K} \left(\hat{B}_{i,i+\mathbf{a}_\nu}^2 + \hat{B}_{i,i-\mathbf{a}_\nu}^2 - \hat{B}_{i,i+\mathbf{a}_\nu} \hat{B}_{i,i-\mathbf{a}_\nu} - \hat{B}_{i,i-\mathbf{a}_\nu} \hat{B}_{i,i+\mathbf{a}_\nu} \right) \right] \\ &= \int d\tau \sum_{i,\nu} \left[\bar{\psi} \partial_\tau \psi + \left(-t \hat{B}_{i,i+\mathbf{a}_\nu} - \frac{\alpha^2}{K} \hat{B}_{i,i+\mathbf{a}_\nu}^2 \right) - \frac{\alpha^2}{K} \left(\hat{B}_{i,i-\mathbf{a}_\nu}^2 - \hat{B}_{i,i+\mathbf{a}_\nu} \hat{B}_{i,i-\mathbf{a}_\nu} - \hat{B}_{i,i-\mathbf{a}_\nu} \hat{B}_{i,i+\mathbf{a}_\nu} \right) \right] \\ &= \int d\tau \sum_{i,\nu} \left[\bar{\psi} \partial_\tau \psi - \left(t \hat{B}_{i,i+\mathbf{a}_\nu} - \frac{2\alpha^2}{K} \hat{B}_{i,i+\mathbf{a}_\nu}^2 \right) + \frac{\alpha^2}{K} \left(\hat{B}_{i,i+\mathbf{a}_\nu} \hat{B}_{i,i-\mathbf{a}_\nu} + \hat{B}_{i,i-\mathbf{a}_\nu} \hat{B}_{i,i+\mathbf{a}_\nu} \right) \right]. \end{aligned}$$

The term $-t \hat{B}_{i,i+\mathbf{a}_\nu} - \frac{2\alpha^2}{K} \hat{B}_{i,i+\mathbf{a}_\nu}^2$ is also obtained in the “bond” SSH (bSSH) model and it produces an effective Heisenberg-like Hamiltonian with an antiferromagnetic $J = 2\alpha^2/K$ [?]. Here, however, we have additional terms proportional to α^2/K . We can expand the products of operators and rearrange terms

$$\begin{aligned}
\frac{\alpha^2}{K} \sum_{i,\nu} \left(\hat{B}_{i,i+a_\nu} \hat{B}_{i,i-a_\nu} + \hat{B}_{i,i-a_\nu} \hat{B}_{i,i+a_\nu} \right) &= -\frac{2\alpha^2}{K} \left[\sum_{i,\nu} \sum_{\sigma} \left(c_{i-a_\nu,\sigma}^\dagger n_{i,\sigma} c_{i+a_\nu,\sigma} + c_{i+a_\nu,\sigma}^\dagger n_{i,\sigma} c_{i-a_\nu,\sigma} \right) \right. \\
&\quad \left. + \sum_{i,\nu} \sum_{\sigma \neq \sigma'} \left(c_{i+a_\nu,\sigma}^\dagger c_{i,\sigma'}^\dagger c_{i,\sigma} c_{i-a_\nu,\sigma'} + c_{i-a_\nu,\sigma}^\dagger c_{i,\sigma'}^\dagger c_{i,\sigma} c_{i+a_\nu,\sigma'} \right) \right] \\
&\quad + \frac{\alpha^2}{K} \sum_{i,\nu} \hat{B}_{i+a_\nu,i-a_\nu},
\end{aligned}$$

where $\hat{B}_{i+a_\nu,i-a_\nu} = \sum_{\sigma} \left(c_{i+a_\nu,\sigma}^\dagger c_{i-a_\nu,\sigma} + \text{h.c.} \right) = \sum_{\sigma} \left(\bar{\psi}_{i+a_\nu,\sigma} \psi_{i-a_\nu,\sigma} + \text{h.c.} \right)$. The first term represents a hopping interaction that allows an electron to hop between next-nearest neighbor sites along the \hat{x} or \hat{y} directions with amplitude $2\alpha^2/K$ depending upon the density of the intermediate site. The second term represents an interaction that shifts a bond pair by one site. The final term allows electrons to hop between next-nearest neighbors along the crystallographic directions with amplitude α^2/K .

Supplementary Note 2: Compressibility and Spectral Weight

To assess the transport properties of the system, we measured the system's compressibility $\kappa = \frac{d\langle n \rangle}{d\mu}$ and local Green's function $\beta G(\mathbf{r} = 0, \tau = \beta/2)$ for an $L = 8$ cluster at $\beta t = 16$. The compressibility $\kappa = 0$ ($\neq 0$) for an insulating (metallic) system. Conversely, the local Green's function provides a measure of the integrated spectral weight near the Fermi energy [?]. Fig. S1a plots the compressibility in the (λ, U) -plane. It is non-zero for $U \lesssim 2$ and $\lambda \lesssim 0.1$ indicating that this region of the phase diagram is metallic at this temperature. $\kappa = 0$ throughout the remainder of the phase diagram. Fig. S1b plots the single particle Green's function. It is also largest in the same region where $\kappa \neq 0$.

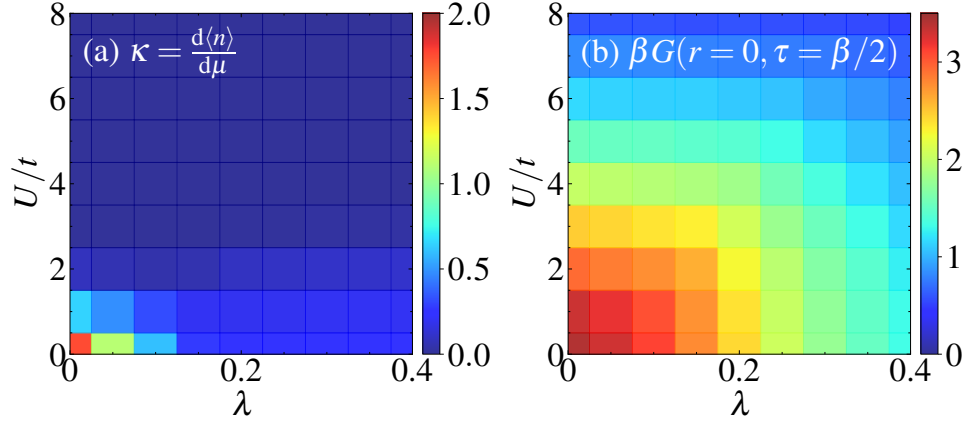


FIG. S1. The (a) compressibility κ and (b) local single particle Green's function $\beta G(\mathbf{r} = 0, \tau = \beta/2)$ for the optical SSH-Hubbard model as a function of λ and U . All results are for an $L = 8$ cluster at $\beta t = 16$ with $\omega/t = 0.5$.

Supplementary Note 3: Correlation Ratios

Figure S2 shows additional correlation ratio crossings for $U/t \in [0, 8]$ as indicated in each panel. Each (a) panel plots the bond-ordered-wave (BOW) correlation ratios while each (b) panel plots the antiferromagnetic (AFM) correlation ratios.

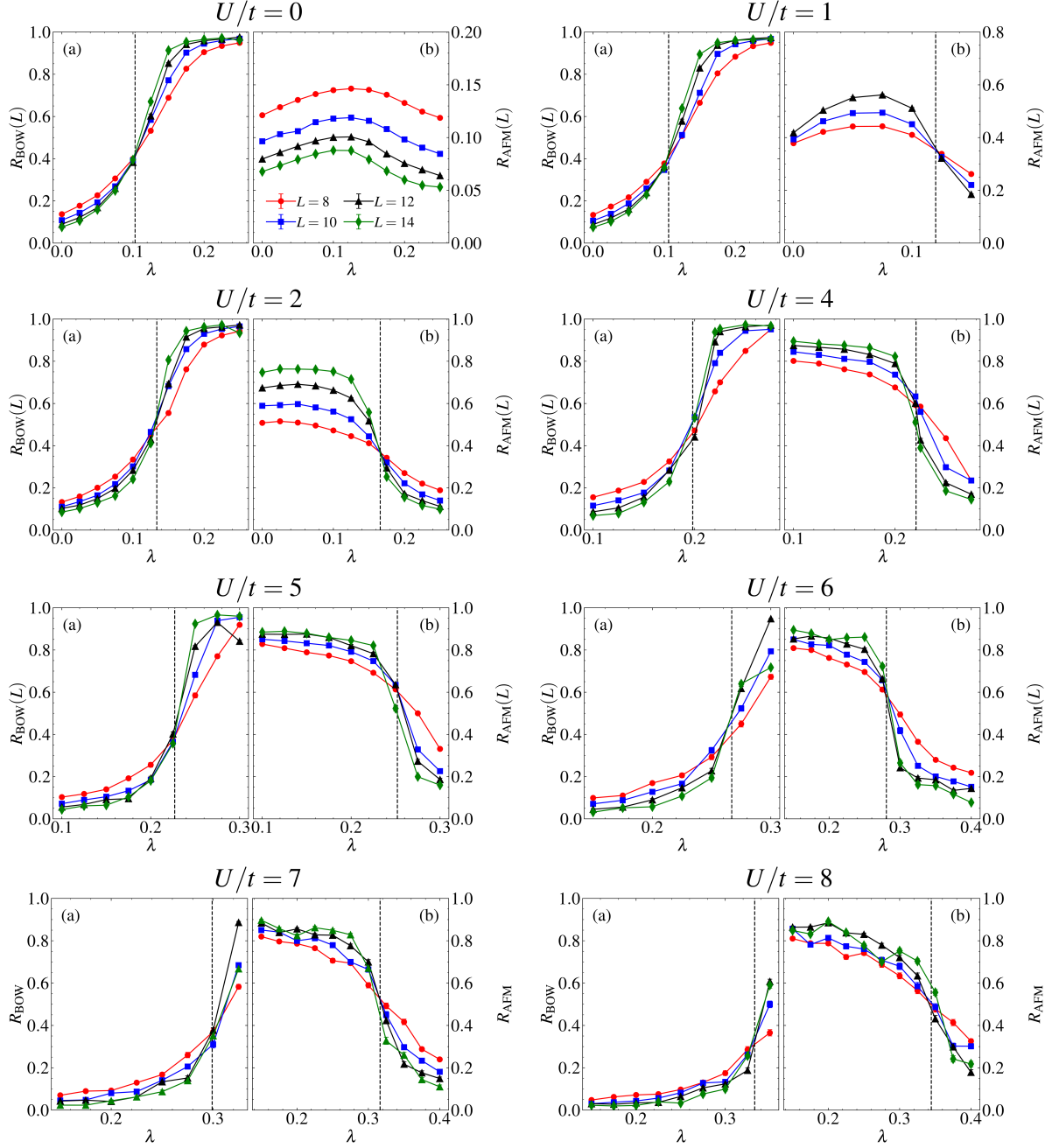


FIG. S2. (a) Bond-ordered-wave and (b) antiferromagnetic (AFM) correlation ratios for $U/t \in [0, 8]$, as indicated in each subplot. The dashed black line indicates the location of the quantum critical point (QCP).

Supplementary Note 4: Antiferromagnetic susceptibility and structure factor

Here we assess the low temperature AFM susceptibility and equal-time structure factors of the pure oSSH model ($U/t = 0$). Figs. S3a and S3b plot the AFM susceptibility χ_{AFM} obtained on an $L = 14$ cluster for $\beta t = 14$ and $\beta t = 28$, respectively, and two different phonon energies. For $\Omega/t = 0.5$, there is a weak enhancement in χ_{AFM} compared to the non-interacting ($\lambda = 0$) case. Increasing the phonon energy to $\Omega/t = 2$ results in a slightly larger enhancement. The dashed lines in each panel indicate the bond-order-wave quantum critical points λ_c^{BOW} for the two phonon frequencies. In this case, χ_{AFM} is suppressed with the onset of long-range BOW order.

Figs. S3c and S3d plot the corresponding structure factor S_{AFM} . Here we also observe a slight increase in the strength of the AFM correlations but the degree of the enhancement is much smaller than in the susceptibility. Since the latter integrates over all imaginary time fluctuations, this behavior is consistent with the presence of increased short-range fluctuating AFM correlations and a lack of long-range magnetic order at this temperature.

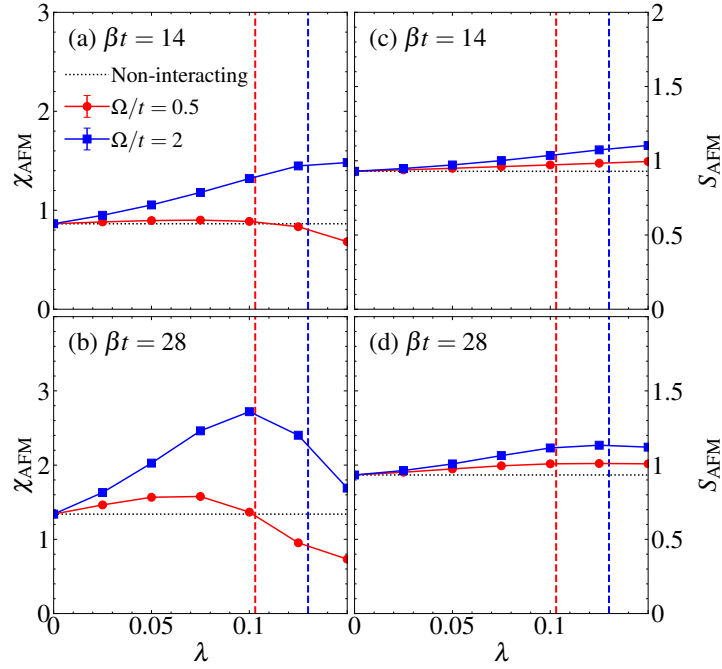


FIG. S3. Antiferromagnetic susceptibility χ_{AFM} for $L = 14$, $\Omega/t = 0.5$ and 2 , $\beta t = 14$ [panel (a)], and $\beta t = 28$ [panel (b)] compared to the non-interacting solution (black dotted line). The vertical dashed lines denote the value of λ_c^{BOW} for each respective phonon frequency. The corresponding antiferromagnetic structure factors S_{AFM} are shown in panels (c) and (d).